THE JOURNAL OF BIOLOGICAL CHEMISTRY VOL. 285, NO. 28, pp. 21724–21735, July 9, 2010

Calcium Oxalate Stone Formation in the Inner Ear as a Result of an *Slc26a4* Mutation*[S]◆

Received for publication, March 7, 2010, and in revised form, April 19, 2010 Published, JBC Papers in Press, May 4, 2010, DOI 10.1074/jbc.M110.120188

Amiel A. Dror[‡1], Yael Politi[§], Hashem Shahin[‡], Danielle R. Lenz[‡], Silvia Dossena[¶], Charity Nofziger[¶2], Helmut Fuchs[‖], Martin Hrabé de Angelis[‖], Markus Paulmichl[¶], Steve Weiner[§], and Karen B. Avraham[‡3]**

*From the [‡]Department of Human Molecular Genetics and Biochemistry, Sackler Faculty of Medicine, Tel Aviv University, Tel Aviv 69978, Israel, the [§]Department of Structural Biology, Weizmann Institute of Science, Rehovot 76100, Israel, the [¶]Institute of Pharmacology and Toxicology, Paracelsus Medical University, A-5020 Salzburg, Austria, the [‖]Institute of Experimental Genetics, Helmholtz Zentrum München, 85764 Neuherberg, Germany, and the **Center of Life and Food Sciences Weihenstephan, Technische Universität München, 85354 Freising, Germany*

Calcium oxalate stone formation occurs under pathological conditions and accounts for more than 80% of all types of kidney stones. In the current study, we show for the first time that calcium oxalate stones are formed in the mouse inner ear of a genetic model for hearing loss and vestibular dysfunction in humans. The vestibular system within the inner ear is dependent on extracellular tiny calcium carbonate minerals for proper function. Thousands of these biominerals, known as otoconia, are associated with the utricle and saccule sensory maculae and are vital for mechanical stimulation of the sensory hair cells. We show that a missense mutation within the *Slc26a4* gene abolishes the transport activity of its encoded protein, pendrin. As a consequence, dramatic changes in mineral composition, size, and shape occur within the utricle and saccule in a differential manner. Although abnormal giant carbonate minerals reside in the utricle at all ages, in the saccule, a gradual change in mineral composition leads to a formation of calcium oxalate in adult mice. By combining imaging and spectroscopy tools, we determined the profile of mineral composition and morphology at different time points. We propose a novel mechanism for the accumulation and aggregation of oxalate crystals in the inner ear.

Biomineralization processes in the human body normally occur in a variety of different tissues, including bones, teeth, and otoconia within the vestibular system of the inner ear. The vestibular system is comprised of five sensory organs. Three cristae connected to semicircular canals are sensitive for angular movement, and the saccule and utricle are sensitive for linear acceleration and gravity. Otoconia are small highly dense calcitic minerals that associate exclusively with the saccule and utricle. Thousands of otoconia, partially embedded in a gelatinous matrix, are supported on the sensory epithelium and serve as an inertial mass that is critical for mechanical stimulation (1, 2). Movement of the otoconial layer through action of gravitational or inertial forces activate the underlying mechanosensory hair cells to generate action potentials that are transmitted to the brain.

The biomineralization process, such as in otoconia formation, involves organic and inorganic components and results in biominerals that differ significantly in morphology and mechanical properties from similar synthetic or geological minerals (3, 4). Otoconia formation occurs outside the cells and therefore depends on secretion of the required assembly components into the endolymphatic spaces (5). Otoconia seeding in mice begins as early as embryonic day (E)14.5 [4] and initiates extensive mineral growth, with the highest rate of calcification at E15–16 (6). By postnatal day (P)7, otoconia achieve their final size and are maintained at progressive ages with a low rate of calcium turnover (7). The main inorganic fraction of otoconia in birds and mammals is calcite ($CaCO_3$), a polymorph of calcium carbonate (2, 8). The organic fraction of otoconia contains several matrix proteins that are critical for the nucleation and mineralization of otoconia. The major core protein is otoconin-90 (Oc90) (also known as otoconin-95; Oc95) (9) and accounts for more than 90% of the organic phase of otoconia. Oc90 is characterized by a high abundance of negatively charged amino acid residues and has two regions of homology with secretory phospholipase A2 (PLA2) (10). The PLA2 domain lacks enzymatic activity but retains calcium binding function (11). It has been proposed that Oc90 is responsible for determining the calcium carbonate polymorph type of otoconia, namely calcite (12). The delicate balance between the organic and inorganic components of otoconia, including their spatial and temporal distribution, determines the growth rate, shape, and composition of the mineral.

Otoconia are subjected to morphological and compositional changes by diverse environmental and genetic factors. Prolonged exposure to medications such as streptomycin results in

* This work was supported by the European Commission FP6 Integrated Projects EuroHear LSHG-CT-2004-512063 and Eumodic 037188 (to K. B. A.) and the Fonds zur Förderung der Wissenschaftlichen Forschung (FWF) Grant P18608-B05 and Grant PIRSES-GA-2008-230661 (to M. P.).

◆ This article was selected as a Paper of the Week.

[S] The on-line version of this article (available at http://www.jbc.org) contains supplemental Figs. S1–S3.

[1] Supported by a Levtzion Fellowship for outstanding doctoral students in the periphery through the Israel Council for Higher Education.

[2] Supported by the Lise Meitner stipend of the Fonds zur Förderung der Wissenschaftlichen Forschung (FWF) (M1108-B11).

[3] To whom correspondence should be addressed. Fax: 972-3-640-9360; E-mail: karena@post.tau.ac.il.

[4] The abbreviations used are: E, embryonic day; P, postnatal day; BPPV, benign paroxysmal positional vertigo; PDS, pendrin; SEM, scanning electron microscopy; D-PBS, Dulbecco's phosphate-buffered saline; EYFP, enhanced yellow fluorescent protein; WT, wild-type; FTIR, Fourier transform infrared.

formation of abnormal giant otoconia (13, 14). Age-related otoconia degeneration is highly abundant and increases the risk for free floating particles (15). Dislocation of otoconia or their broken particles outside their native position can lead to severe vestibular dysfunction in humans. Benign paroxysmal positional vertigo (BPPV) patients suffer from severe dizziness. This clinical condition affects up to 9% of the population older than 65 years of age (16). The phenotype manifests itself when otoconia migrate to one of the cristae (cupulolithiasis) or the semicircular canals (canalithiasis) and hinders its mechanical sensory properties (17). BPPV is one of the major clinical conditions attributed to dislocated otoconia.

In the current study, we identified and characterized a new recessive mouse mutant named loop (gene symbol *Slc26a4*^{loop}), which carries a recessive missense mutation in the *Slc26a4* gene encoding pendrin. Human mutations in *SLC26A4* lead to a non-syndromic (DFNB4) and syndromic form of deafness with enlargement of the thyroid gland (Pendred syndrome) (18, 19). Mimicking the human pathology and similar to the knock-out mouse model (*Pds*$^{-/-}$) (31), loop mice are profoundly deaf and show abnormal vestibular behavior. Here we present the discovery of a new type of giant mineralized bodies with the composition of calcium oxalate within the *Slc26a4*$^{loop/loop}$ saccule. These mineralized bodies are highly distinct from calcitic wild-type otoconia and have not been previously described in the inner ear. Interestingly, these unique pathological oxalate ear stones are only formed within one out of the two separate compartments of otoconia formation, the utricle and saccule. In our study, we analyzed the wide spectrum of mineral composition in the *Slc26a4*$^{loop/loop}$ inner ear that undergoes dramatic differential changes and provide insight into an abnormal mineralization mechanism in the presence of a genetic mutation.

EXPERIMENTAL PROCEDURES

Mice—All procedures involving animals met the guidelines described in the National Institutes of Health Guide for the Care and Use of Laboratory Animals and have been approved by the Animal Care and Use Committees of Tel Aviv University (M-07-061). The gene symbol, *loop*, was approved by the Mouse Genome Informatics (MGI) International Committee on Standardized Genetic Nomenclature for Mice.

Analysis of Mutation in Slc26a4^{loop} *Mice*—A standard chromosomal mapping procedure was conducted as described previously utilizing polymorphic markers (20). Prediction of the transmembrane helices in the pendrin protein was conducted with two web-based algorithms, the TMHMM Server 2.0 (60) and the SPLIT 4.0 server (61). The ConSeq Server algorithm (62) was used for calculation of conservation scores for each residue. Auditory brainstem response test was performed according to standard protocols for hearing evaluation in mice (21).

Primary Antibodies—For immunohistochemistry and immunoblotting, we used previously characterized polyclonal antibodies as follows: pendrin (22), kindly provided by Jørgen Frøkiær; otoconin-90 (9) and otogelin (23), kindly provided by Christine Petit.

Inner Ear Dissection—Whole inner ears were dissected from newborn and adult mice. To assure fast penetration of fixative into the inner ear labyrinth, the middle ear ossicles were removed to expose the oval window, and a small hole at the top of the cochlea (near the helicotrema) was made by removing portion of the cartilage/bone according to age.

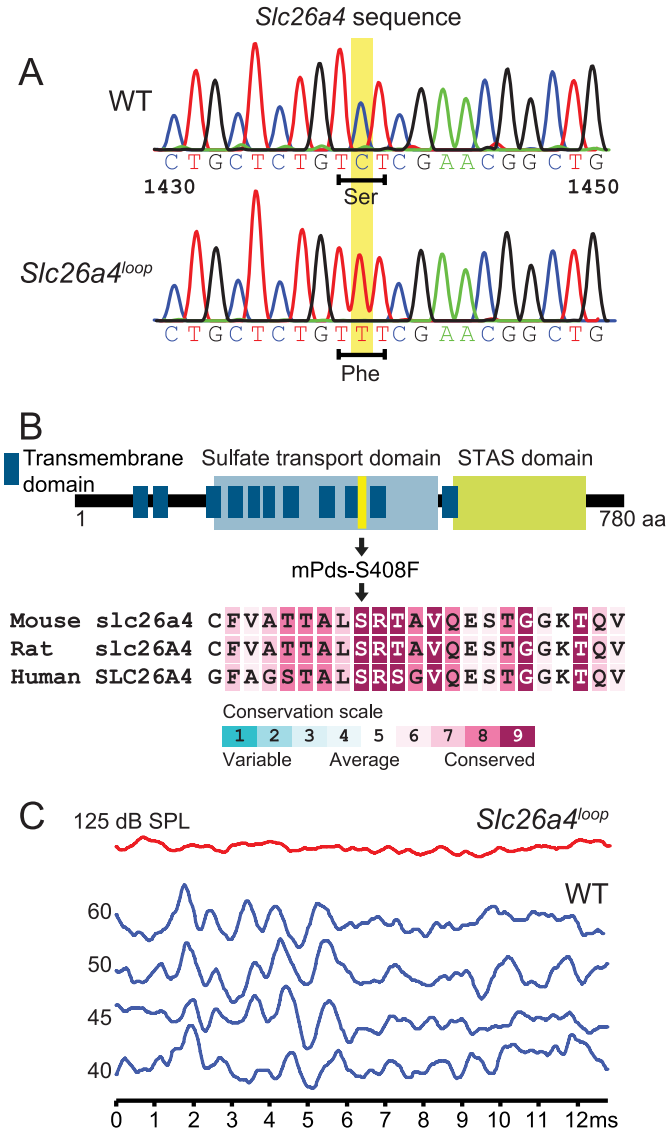

FIGURE 1. **The S408F mutation resides within a highly conserved region of the pendrin protein and leads to deafness and vestibular dysfunction.** *A* and *B*, sequencing of *Slc26a4* from *loop* homozygote cDNA revealed a C to T (c.C1439T) mutation causing a serine to phenylalanine amino acid (*aa*) substitution at position 408 (p.S408F) of the pendrin protein. A hypothetical predicted topology model of pendrin suggests that the pendrin mutation resides in the ninth transmembrane domain. *STAS*, sulphate transporter and anti-sigma factor antagonist. ConSeq analysis shows that the *loop* mutation position is within a highly conserved amino acid with the highest value of nine. *mPds*, mouse Pds. *C*, auditory brainstem response test on 8-week-old mice reveals that *Slc26a4*^{loop} mutants are profoundly deaf according to three frequencies that were tested, 8, 16, and 32 kHz. Output graphs from the 16-kHz examination are shown. $n = 21$.

Scanning Electron Microscopy (SEM)—Fixation of whole inner ears was done in 2.5% glutaraldehyde (Electron Microscopy Sciences) in 0.1 M sodium phosphate buffer for 4 h on ice. After three washes with 0.1 M phosphate buffer, further fine dissections were made to expose the vestibular sensory organs. The samples were run through the osmium tetroxide/thiocarbohydrazide method (24). Briefly, three 1-h incubations in 1% osmium tetroxide were done, separated by 20-min incubations

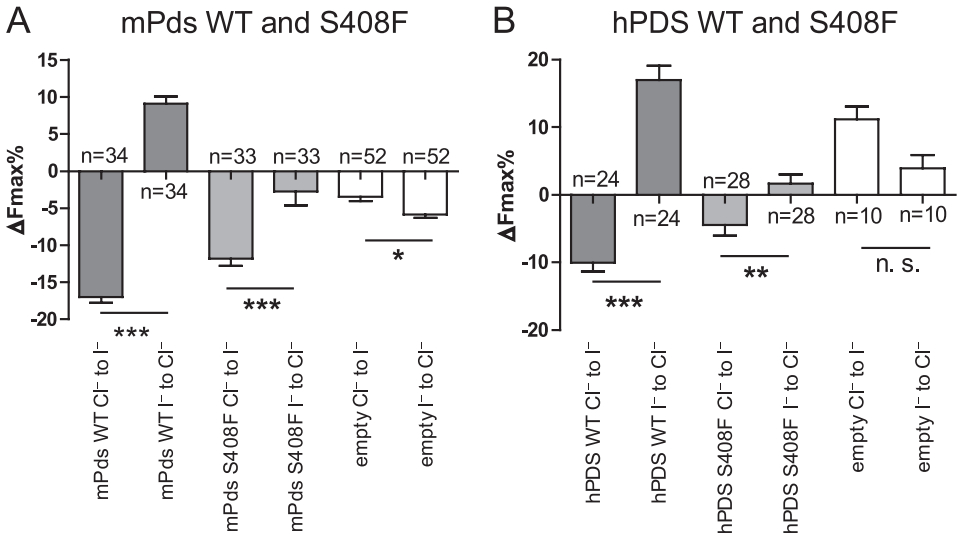

FIGURE 2. **The S408F mutation causes a significant reduction of the related anion transport tested for the mouse pendrin (*A*), as well as for the human pendrin (*B*).** *A*, change of the fluorescence signal (expressed as maximal fluorescence variations, ΔF_{max}%) after the Cl^- to I^- or I^- to Cl^- substitutions (for details, see "Experimental Procedures") in HEK 293 Phoenix cells expressing only the EYFP protein (*empty*) or the EYFP protein and mouse wild-type pendrin (*mPds WT*) or mutated mouse Pds (*mPds S408F*). The numbers of the experiments are given (*n*). Error bars indicate the S.E. Statistical analysis: ***, $p < 0.001$; *, $= p < 0.05$; paired Student's *t* test. *Error bars* indicate S.E. *B*, change of the fluorescence signal (expressed as maximal fluorescence variations, ΔF_{max}%) after the Cl^- to I^- or I^- to Cl^- substitutions (for details, see "Experimental Procedures") in HEK 293 Phoenix cells expressing only the EYFP protein (*empty*) or the EYFP protein and human wild-type PDS (*hPDS WT*) or mutated human PDS (*hPDS S408F*). The numbers of the experiments are given (*n*). Error bars indicate the S.E. Statistical analysis: ***, $= p < 0.001$; **, $= p < 0.01$; *n. s.* = not significant; paired Student's *t* test. *Error bars* indicate S.E. The results of the analysis of variance test with Bonferroni's multiple comparison post-test are reported under "Results." *n* represents the number of cells.

in a saturated solution of thiocarbohydrazide. The samples were dehydrated in gradients of ethanol, critical point-dried, and coated with gold for 45 s at 20 mA. For mineral analysis, the mineralized bodies were isolated and dried under a bright light (100 watts) for 24 h. After mounting on carbon tape, the samples were coated with gold for 30 s at 20 mA. Images were acquired with a JEOL JSM-6701F SEM.

Immunohistochemistry (Whole Mount)—Inner ear fixation was done in 4% paraformaldehyde (Electron Microscopy Sciences) in Dulbecco's phosphate-buffered saline (D-PBS) overnight at 4 °C. After three washes in D-PBS, further fine dissections were conducted for isolation of utricle, saccule, crista, and spiral ligament. For permeabilization and blocking, tissues were immersed for 2 h in a D-PBS medium containing 0.2% Triton X-100 and 10% normal donkey serum. Tissues were incubated overnight at 4 °C with pendrin antibody diluted in D-PBS (1:100). Immunolabeling was visualized with an Alexa Fluor 488-conjugated donkey anti-rabbit antibody (diluted 1:200; Invitrogen) together with rhodamine phalloidin (diluted 1:300; Invitrogen), an actin fluorescent dye. After three washes in D-PBS, the samples were mounted on glass slides using ProLong gold antifade reagent (Invitrogen). Confocal laser microscopy was carried out with a Leica TCS SP5 laser confocal microscope.

Immunohistochemistry (Paraffin Sections)—P15 inner ear fixation was done in 4% paraformaldehyde (Electron Microscopy Sciences) in D-PBS for 4 h at 4 °C. Inner ear decalcification was carried out using 10% EDTA and 4% paraformaldehyde in D-PBS, pH 7.4, for 3 days at 4 °C. After three washes in D-PBS, tissues were dehydrated and embedded in paraffin. Sections of 10 μm were cut using a rotary microtome (Leica). The sections were dewaxed in xylene and rehydrated. Antigen retrieval was accomplished by submerging the slides in unmasking solution (Vector Laboratories) and heating in a microwave oven for 4 min. To block nonspecific binding, the slides were transferred into PBS-D medium containing 0.2% Triton and 0.2% gelatin. Slides were incubated overnight at 4 °C with otoconin-90 and otogelin antibodies diluted in antibody dilution buffer (1:200). Immunolabeling was visualized with an Alexa Fluor 568-conugated donkey anti-rabbit antibody (diluted 1:200; Invitrogen). Staining with 4′-6-diamidino-2-phenylindole was used for the visualization of the cell nucleus. After three washes in D-PBS, the samples were mounted with a coverslip using ProLong gold antifade reagent (Invitrogen). Confocal laser microscopy was carried out with a Leica TCS SP5 laser confocal microscope.

Histology—Paraffin sections were dewaxed in xylene and rehydrated. A standard hematoxylin and eosin staining procedure was performed to reveal the histology and morphology of the inner ear.

Protein Extraction and Analysis—Western blot was conducted following a previously described protocol for protein extraction from otoconia (9). Briefly, inner ears were dissected out from P15 mice following prompt isolation of utricle for further processing. The soluble protein extract was assayed for protein content with the Bradford assay (Sigma). Tissue samples were homogenized and fractionized into three different fractions. To expose the organic fraction of the crystals for immunoblotting, the mineral pellet was decalcified overnight in 20% EDTA, pH 7.4. For analysis of proteins in the mineral fraction, gel loading was based on fixed volumes of samples that contained proteins extracted from six utricles from each genotype.

Cloning of Human and Mouse Pendrin (PDS) and the Respective Mutants Used in the Functional Studies—The procedure used to clone the open reading frame of the human *PDS* gene into the bicistronic expression vector pIRES2-EYFP, a modification of the pIRES2-EGFP (Clontech), was described in detail previously (25). A similar approach was used to clone the open reading frame of the mouse *Pds* gene into the bicistronic expression vector pIRES2-EYFP. Both the mouse and the human *PDS*, as well as the enhanced yellow fluorescent protein (EYFP), were translated separately from a single bicistronic mRNA expressed under the control of the cytomegalovirus promoter. The mutant human and mouse PDS S408F were generated by the PCR-based site-directed mutagenesis method using the QuikChange® Site-Directed Mutagenesis

Kit (Stratagene), with the following primers: human PDS, forward, 5′-GGCCACCACTGCTCTTTTCCGCACGGCC-GTCCAGG-3′; human PDS, reverse, 5′-CCTGGACGGCC-GTGCGGAAAAGAGCAGTGGTGGCC-3′; mouse PDS, forward, 5′-CTACCACTGCTCTGTTTCGAACGGCTGT-CCAGGAG-3′; mouse PDS, reverse, 5′-CTCCTGGACAG-CCGTTCGAAACAGAGCAGTGGTAG-3′. All constructs were verified by sequencing of the complete open reading frame.

Cell Culture and Transient Transfection—HEK 293 Phoenix cells (a second generation retrovirus-producing cell line for the generation of helper-free ecotropic and amphotropic retroviruses (26)) were grown in Eagle's minimum essential medium (Sigma) supplemented with 10% fetal bovine serum (Cambrex BioScience), 2 mM L-glutamine, 100 units/ml penicillin, 100 μg/ml streptomycin, and 1 mM pyruvic acid (sodium salt). The cells were maintained at 37 °C in a 5% CO_2, 95% air-humidified incubator. Subcultures were routinely established every 2nd to 3rd day into Petri dishes (Ø 10 cm) after trypsin/EDTA treatment. For *in vivo* functional fluorometric assays, HEK 293 Phoenix cells were transiently transfected with plasmids expressing EYFP and human or mouse wild-type (WT) PDS, human or mouse PDS S408F, or only EYFP (control) by calcium-phosphate precipitation. One day before transfection, cells were seeded on 6-well plates (Ø 35 mm) and grown to 60–80% confluency. For each well, 3 (for human PDS) or 4.5 μg (for mouse PDS) of plasmid dissolved in a final volume of 67.5 μl of H_2O were mixed with 7.5 μl of buffer A (2.5 M $CaCl_2$) and 75 μl of buffer B (140 mM NaCl, 1.5 mM Na_2HPO_4, 50 mM HEPES, pH 7.05, adjusted with NaOH) and incubated 10–15 min at room temperature. The transfection mix was added to complete growing medium and applied to the cells. For the fluorescence measurements, cells were split on round, poly-L-lysine-coated coverslips (Ø 15 mm) 24 h after transfection. Measurements were performed 48–56 h after transfection.

Fluorometric Analyses—The fluorometric method was described previously in detail (25, 27–29). Briefly, to evaluate pendrin-induced ion transport, HEK 293 Phoenix cells were transfected with plasmids encoding for human or mouse WT PDS and EYFP, human or mouse PDS S408F and EYFP, or with the empty plasmid encoding for EYFP only. The cells were continuously perfused in a laminar flow chamber (flux speed 0.8–1.0 ml/min) with "isotonic high Cl^-" (2 mM KCl, 135 mM NaCl, 1 mM $MgCl_2$, 1 mM $CaCl_2$, 10 mM D-glucose, 20 mM HEPES, pH 7.4; 308 mosM with mannitol) or "isotonic high I^-" (2 mM KCl, 135 mM NaI, 1 mM $MgCl_2$, 1 mM $CaCl_2$, 10 mM D-glucose, 20 mM HEPES, pH 7.4; 308 mosM with mannitol) solutions. By changing the isotonic high Cl^- to isotonic high I^- solution, iodide influx can be measured, whereas the iodide efflux can be estimated by switching back from isotonic high I^- to isotonic high Cl^- solution. EYFP fluorescence intensity is able to reveal changes in the intracellular halide concentration; as iodide is a much better EYFP quencher than chloride (30), an increase of intracellular iodide leads to a decrease of EYFP fluorescence. As a consequence, a fluorescence decrease indicates an iodide influx, whereas a fluorescence increase indicates an iodide efflux. The EYFP fluorescence measurements were performed using a Leica TCS SP5 AOBS confocal microscope (Leica Microsystems), using a 514 nm argon laser line for exciting the EYFP fluorescence. Fluorescence time courses were obtained by analyzing regions of interest within single cells. Measurements were started after steady-state conditions were reached. Maximal fluorescence variations (ΔF_{max}%) represent the maximal observed percentage difference with respect to the fluorescence intensity at the moment of the solution substitution (iodide/chloride). Data were collected from 3 (for mouse PDS) or 2 (for human PDS) independent experimental days. Experiments were performed at room temperature.

Statistical analysis was assessed by one-way analysis of variance with the Bonferroni's multiple comparison post-test or with the paired Student's t test. Statistical significant differences were assumed at p values < 0.05.

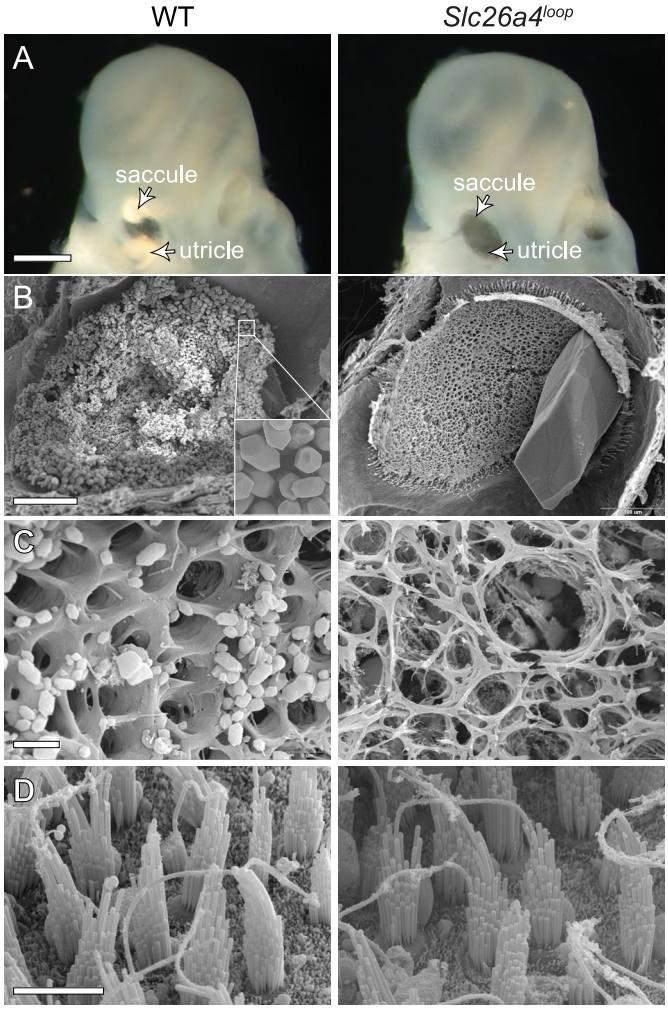

FIGURE 3. **Gross malformation of the vestibular gravity receptor.** *A*, wild-type otoconia can be easily detected under a light microscope when looking at isolated inner ears. Two bright reflected areas represent the otoconia of the saccule and utricle of newborn mice. *Slc26a4^{loop}* mutant mice lack the bright reflection, and instead, a dark hole appears when looking through the oval window (*arrowheads*). *B*, SEM of 2-month-old utricle shows thousands of otoconia (*inset*) that cover the sensory epithelium in a wild-type mouse, whereas a giant stone is appearing at *Slc26a4$^{loop/loop}$* utricle. *C*, imaging of the gelatinous matrix (otoconial membrane) reveals its normal structure in wild-type mice, which is characterized by typical pores. In *Slc26a4^{loop}* mutants, the otoconial membrane is dissociated and severed. *D*, high resolution images of the underlying hair cells show that *Slc26a4$^{loop/loop}$* vestibular hair cells appear to be normal. *Scale bars* equal 500 μm in *panel A*, 100 μm in *B*, 5 μm in *C* and *D*. $n = 4$.

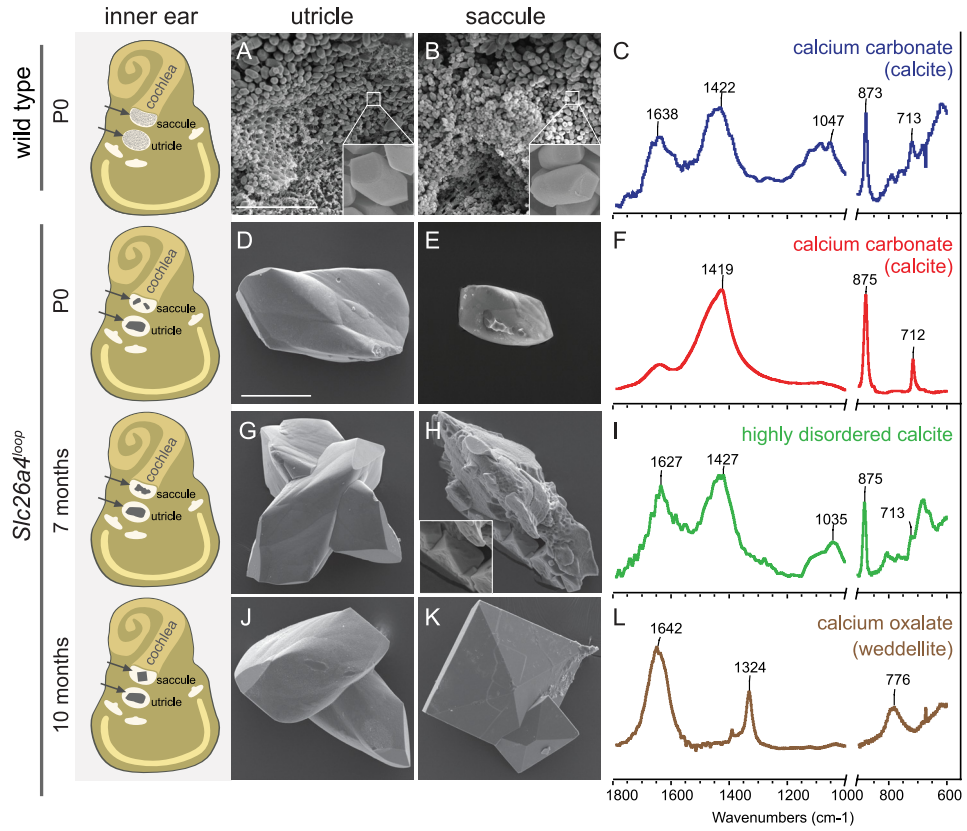

FIGURE 4. **Mineral morphology and composition across different progressive stages.** A schematic illustration of the inner ear summarizing the morphological differences of the ear stones at three time points, P0, 7 months, and 10 months, is shown (*left panel*). *Left* and *right panel*, SEM images of the minerals from the utricle (*left panel*) and saccule (*right panel*). *A* and *B*, otoconia from wild-type mice. The image shows the small (~7 μm) otoconia with typical morphology (*inset* in *A* and *B*). *D* and *E*, minerals extracted from the utricle (*D*) and saccule (*E*) of newborn *Slc26a4*^{loop} mutant mice. The utricle minerals are larger; both types have altered morphology relative to wild-type otoconia and show smooth surfaces. *G* and *H*, minerals extracted from 7-month-old *Slc26a4*^{loop} mutant mice. Although in the utricle, no changes can be observed as compared with the minerals of newborn mice, the saccule contained an abnormal giant stone with a variety of morphological characteristics. SEM images showed that parts of this stone resemble the morphology of weddellite, calcium oxalate dihydrate (*inset* in *H*). *J* and *K*, minerals extracted from 10-month-old *Slc26a4*^{loop} mutant mice. The minerals in the utricle appear similar to the minerals found at earlier stages (*J*). In the saccule, a new type of mineral can be found instead of the giant calcitic crystals observed earlier. These minerals have a crystal morphology typical of calcium oxalate dihydrate (weddellite) crystals. *C*, *F*, *I*, and *L*, normalized FTIR spectra of minerals extracted from the saccule and utricle at different developmental stages. The parts of the spectra in the range below 1000 cm^{-1} are expanded to reveal the details. *C*, wild-type crystals. The spectrum of wild-type otoconia shows the typical calcite vibrations at 713, 875, and 1422 cm^{-1}. The spectrum also shows large contribution from organic components at 1638 and around 1047 cm^{-1}. *F*, spectrum of the mineral extracted from the saccule and utricle in newborn *Slc26a4*^{loop} mutant mice. *I*, spectrum of the mineral extracted from the saccule in *Slc26a4*^{loop} mutant mice at the age of 7 months. Note broadening of the peak at 713 cm^{-1}. *L*, spectrum of the mineral extracted from the saccule in *Slc26a4*^{loop} mutant mice at the age of 10 months. Vibrations at 1324 and 776 cm^{-1} are typical of weddellite crystals. *Scale bars* equal 50 μm in *panels A* and *B*; *scale bars* equal 100 μm in *panels D*, *E*, *G*, *H*, *J*, and *K*. $n \geq 15$.

Fourier Transform Infrared (FTIR) Spectroscopy—Otoconia of wild-type mice and giant minerals from *Slc26a4*^{loop} mutant mice were extracted by finely dissecting the vestibular apparatus and isolating the crystals from the saccule and utricle. The ground crystals were mixed with KBr powder in an agate mortar and pestle. KBr pellets were prepared and analyzed by FTIR spectrometer (Nicolet 380). Calcite spectra were normalized to the intensity of the peak at 875 cm^{-1}. Weddellite spectrum was normalized to the intensity of the peak at 1324 cm^{-1}. For each time point, pooled harvested minerals ($n \geq 15$) were subjected to FTIR spectroscopy analyses that confirmed its composition. Three biological and technical repeats were performed for each type of mineral.

Raman Spectroscopy—Individual isolated otoconia were selected for measurement under a Leica light microscope. Raman spectra were acquired using a Renishaw Raman imaging microscope with a diode (780 nm) laser beam. *X-X* spectra of each stone/stone type were averaged. Five single mineralized bodies for each type of mineral were analyzed.

RESULTS

Slc26a4 Mutation Leads to Deafness and Severe Balance Defects—The loop mouse originated in an *N*-ethyl-*N*-nitrosourea (ENU) mutagenesis screen for neurosensory disorders (63). Chromosomal mapping revealed that the recessive *loop* mutation localized to the region of chromosome 12 where *Slc26a4* resides (supplemental Fig. S1). Sequencing of this gene from *loop* homozygote cDNA revealed a C to T transition (c.C1223T) causing a serine (aromatic) to phenylalanine (polar) amino acid substitution at position 408 (p.S408F) (Fig. 1*A*). Several topology models for pendrin have been suggested in the literature, although the number of potential transmembrane domains remains ambiguous (28). According to our prediction, Ser-408 is buried in a hydrophobic signature of pendrin within the ninth transmembrane domain (Fig. 1*B*). Furthermore, multiple sequence alignment analysis of 300 homologous sequences using the ConSeq Server revealed that Ser-408 resides within a highly conserved domain of pendrin, ranked with the highest conservation score (Fig. 1*B*).

To evaluate the hearing of *Slc26a4*^{loop} mice, a 20-kHz sound burst at 100 db, a Preyer reflex test, was introduced to 8-week-old mice. A typical Preyer reflex was absent in all *Slc26a4*^{loop} mice tested. To further investigate the hearing of these mice, auditory brainstem response was performed and demonstrated that *Slc26a4*^{loop} mice are profoundly deaf at all frequencies tested (32, 16, and 8 kHz) (Fig. 1*C*). In addition to the auditory deficiency, the *Slc26a4*^{loop} mice exhibited variable vestibular deficits such as unsteady gait, circling, absence of reaching response, and tilted body.

Functional Characterization of Mouse and Human Wild-type PDS and S408F—Pendrin localization in the inner ear is not affected by the S408F mutation (supplemental Fig. S2). To

test the functional (ion transport) properties of the mouse WT pendrin (Pds) and its S408F mutation, we used a fast fluorometric method for measuring anion transport (27, 29). With this technique, Pds-mediated anion flux is measured by monitoring the I^-- and Cl^--induced quenching of the enhanced yellow fluorescent protein (EYFP) fluorescence signal (see "Experimental Procedures"). As iodide is a much better quencher of EYFP fluorescence than chloride (30), in our experimental design, a fluorescence decrease indicates an iodide influx, whereas a fluorescence increase indicates an iodide efflux. HEK 293 Phoenix cells expressing mouse WT Pds show a marked halide transport activity. The change in fluorescence in cells transfected with both EYFP and mouse Pds or EYFP alone (the empty vector, used as control) were measured after a Cl^- to I^- substitution in the extracellular bathing saline (from isotonic high Cl^- to isotonic high I^- solution) followed by an I^- to Cl^- substitution (from isotonic high I^- to isotonic high Cl^- solution). The expression of WT mouse Pds leads to a marked decrease (Cl^- to I^- substitution) or increase (I^- to Cl^- substitution) in EYFP fluorescence intensity (Fig. 2*A*; *mPds WT*), indicating a substantial I^- influx and I^- efflux, respectively. The transport values (ΔF_{max}%) of mouse WT Pds are: -17.0 ± 0.8, $n = 34$ (Cl^- to I^- substitution) and $+9.1 \pm 1.0$, $n = 34$ (I^- to Cl^- substitution). These values are significantly different from each other ($p < 0.001$) and from the control (Cl^- to I^- substitution, $\Delta F_{max}\% = -3.4 \pm 0.6$, $n = 52$, $p < 0.001$ *versus* WT Pds; I^- to Cl^- substitution, $\Delta F_{max}\% = -5.8 \pm 0.5$, $n = 52$, $p < 0.001$ *versus* WT PDS).

Similarly to WT Pds, the expression of mouse Pds S408F in HEK 293 Phoenix cells leads to a decrease (Cl^- to I^- substitution) in EYFP fluorescence intensity ($\Delta F_{max}\% = -11.8 \pm 1.0$, $n = 33$), which is statistically different from control ($p < 0.001$; Fig. 2*A*). However, the reduction is statistically lower ($p < 0.01$) as compared with that with WT Pds. The I^- efflux (I^- to Cl^- substitution), in contrast, is heavily impaired ($\Delta F_{max}\% = -2.7 \pm 1.9$, $n = 33$, $p < 0.001$) as compared with WT Pds and not significantly different from the control. Therefore, these data indicate that the anion exchange activity of mouse Pds S408F is compromised.

The S408F mutation has not been reported in humans. However, we were interested to know whether or not the corresponding mutation in human PDS is also able to affect the transport function. HEK 293 Phoenix cells expressing human WT PDS also show marked halide transport activity (Fig. 2*B*), which is similar to that reported earlier (29). The expression of human WT PDS leads to a marked decrease (Cl^- to I^- substitution, $\Delta F_{max}\% = -10.0 \pm 1.3$ $n = 24$) or increase (I^- to Cl^- substitution, $\Delta F_{max}\% = +17.0 \pm 2.1$ $n = 24$) in EYFP fluorescence intensity, indicating an I^- influx and I^- efflux, respectively. These values are significantly different from each other ($p < 0.001$) and from the control (Cl^- to I^- substitution, $\Delta F_{max}\% = +11.1 \pm 1.9$, $n = 10$, $p < 0.001$; I^- to Cl^- substitution, $\Delta F_{max}\% = +3.9 \pm 2.0$, $n = 10$, $p < 0.001$).

The expression of human PDS S408F in HEK 293 Phoenix cells leads to a significant iodide influx (Fig. 2*B*) (Cl^- to I^- substitution, $\Delta F_{max}\% = -4.5 \pm 1.5$, $n = 28$, $p < 0.001$ as compared with control). However, the I^- efflux (I^- to Cl^- substitution) is heavily impaired ($\Delta F_{max}\% = +1.7 \pm 1.3$, $n = 28$, $p <$ 0.001) as compared with WT. This finding is similar to that obtained with the respective mouse mutant. These data demonstrate that the mouse S408F leads to the same impaired functional phenotype when studied with respect to the human PDS sequence.

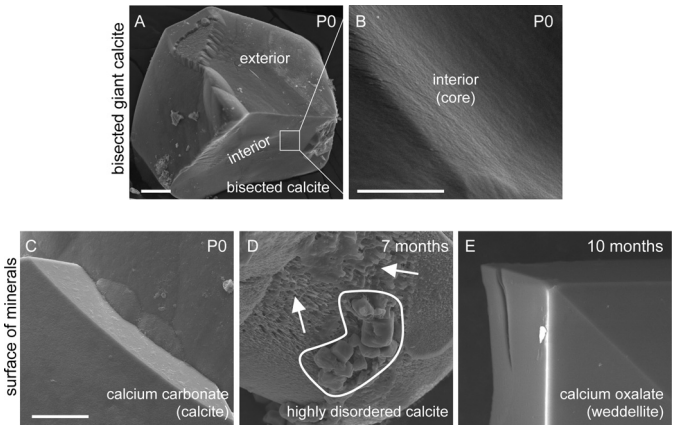

FIGURE 5. **Ultrastructural morphology of the surface and core of *Slc26a4*$^{loop/loop}$ mineralized bodies.** *A* and *B*, bisected calcite minerals of P0 utricle. *A*, the interior facet of bisected mineral shows a smooth surface similar to the exterior surface of the mineral. *B*, high magnification of the interior surface. *C–E*, surface of different mineralized bodies isolated from *Slc26a4*$^{loop/loop}$ saccule presented with high power SEM images. *C*, calcium carbonate (calcite) minerals of P0 mice have a smooth and clean surface. *D*, highly disordered calcite minerals of 7-month-old saccules revealed a surface that is pitted and fissured (*arrows*). This stone contained domains that resemble the morphology of calcium oxalate in the form of weddellite (*circled*). *E*, calcium oxalate (weddellite) mineral of 10-month-old saccules show a smooth and clean surface. *Scale bars* equal 25 μm in *panel A*, 5 μm in *panel B*, and 10 μm in *panels C–E*. $n = 6$.

Pendrin S408F Mutation Leads to Gross Morphological Malformation of the Vestibular Sensory Maculae—A detailed phenotypic characterization of the vestibular sensory maculae was performed to reveal the pathology underlying the aberrant vestibular behavior of the *Slc26a4*^{loop} mutants. Comparison between wild-type and *Slc26a4*^{loop} P0 inner ears under a binocular shows that the mutant lacks the calcitic otoconia of the utricle and saccule that are represented by bright reflected areas in the control (Fig. 3*A*, *arrows*). Examination of finely dissected utricles of 2-month-old mice using high resolution SEM shows thousands of otoconia (~5 μm) in wild-type utricle, whereas in *Slc26a4*$^{loop/loop}$ mice, one giant stone (~300 μm) is apparent (Fig. 3*B*). The organic gelatinous matrix (otoconial membrane) that natively supports the otoconia load is degenerated in *Slc26a4*^{loop} mutants (Fig. 3*C*). Despite the severe deformation of the extracellular components, the hair cells of the sensory epithelium appear to be normal in *Slc26a4*^{loop} mutant mice, presenting the typical hair bundle structure with a staircase stereocilia organization (Fig. 3*D*). The normal morphology of utricular hair cells in 2-month-old *Slc26a4*$^{loop/loop}$ mice is a prominent difference in comparison with the *Pds*$^{-/-}$ mice, which show severe utricular hair cell degeneration already at the age of 1 month (31).

Giant Calcium Oxalate Stones Are Formed in Slc26a4$^{loop/loop}$ *Vestibular System*—Investigation of the formation of the aberrant giant stones across different progressive ages reveals differential mineralization changes between utricles and saccules. By combining an SEM imaging technique with Raman and

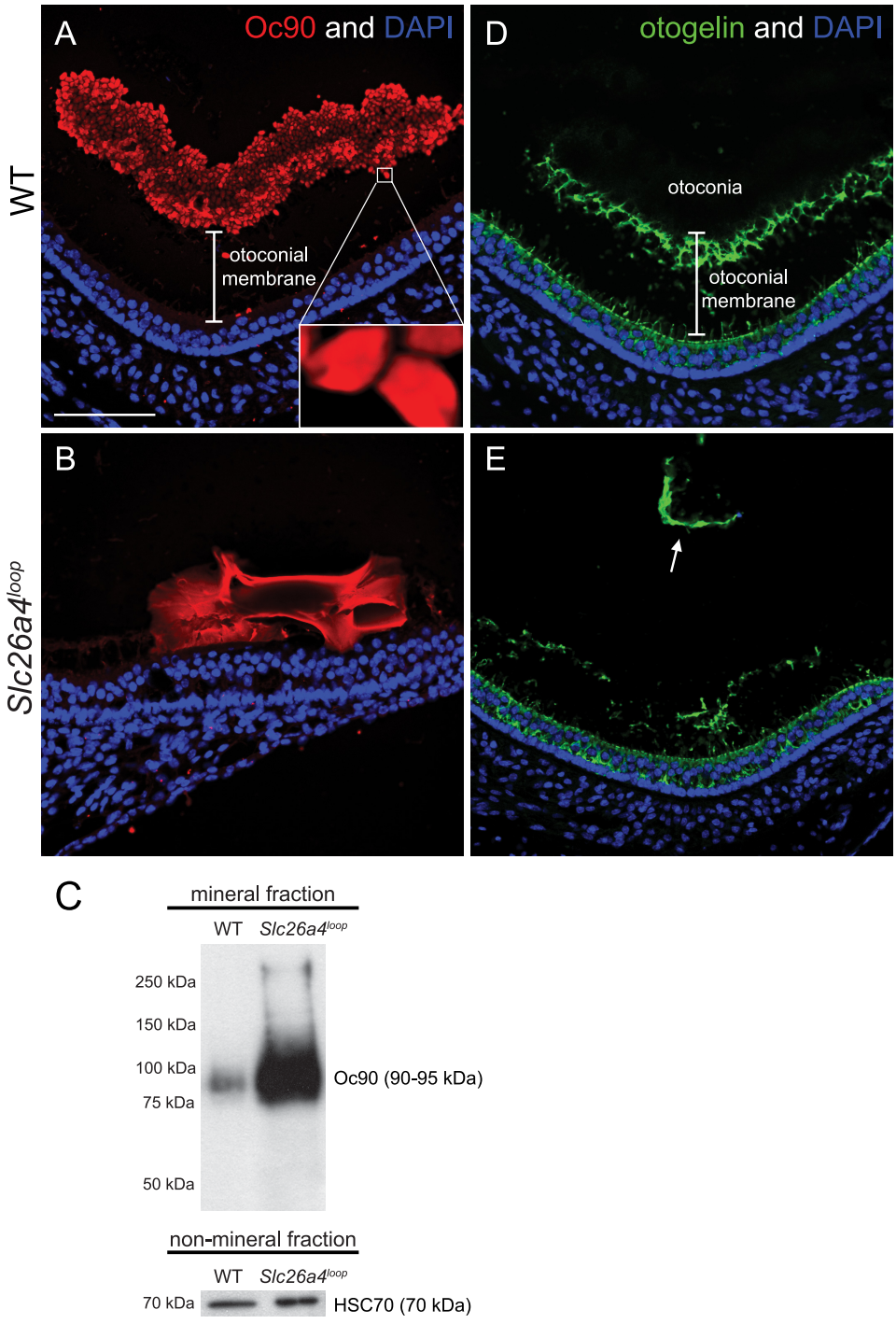

FIGURE 6. **Oc90 conglomerates assemble the core of the calcitic giant minerals.** *A* and *B*, Oc90 immunostaining on P15 paraffin sections of decalcified inner ears. *A*, wild-type otoconia are labeled with Oc90 (*red*) and highlight the boundaries of each otoconium. The unlabeled gap between the sensory epithelium (nuclei) and the otoconia represents the gelatinous matrix (otoconial membrane) that supports the otoconia load. *B*, a Oc90 (*red*) conglomerate is present in the giant calcitic mineral. Unlike the smooth expression of Oc90 in a single otoconium (*inset* in *A*), in the giant mineral, Oc90 expression has different levels of intensity along the mineral body. Furthermore, the giant mineral resides directly on the sensory epithelium, and the gap that corresponds to the otoconial membrane is absent. *C*, Western blot analysis of Oc90 in the mineral fraction shows a dramatic increase of protein content in the giant minerals. As a control, the non-mineral fraction was loaded on a gel and labeled with HSC70, confirming the equal amount of pooled utricles that were analyzed in each sample. *D* and *E*, otogelin immunostaining on P15 paraffin sections of decalcified inner ears. *D*, in wild-type mice, otogelin (*green*) is expressed by the supporting cells of the sensory epithelium. The secreted otogelin participates in the otoconial membrane assembly and maintenance. *E*, in *Slc26a4*^{loop} mutant mice, otogelin is expressed by supporting cells; however, the otoconial membrane is severed, disorganized and displaced (*arrow* in *D*). *Scale bars* equal 75 μm in *panels A–D*. $n = 5$.

infrared spectroscopy analyses, we were able to determine the morphology and the composition of the different minerals at the examined stages. A schematic illustration of the inner ear summarizing the morphological differences of the ear stones at three time points (P0, 7 months, and 10 months) is shown (Fig. 4, *left panel*). The wild-type otoconia within the utricle (Fig. 4*A*) and saccule (Fig. 4*B*) have similar morphologies, namely a barrel shape with three terminal rhombohedral faces (Fig. 4, *A* and *B*, *insets*) and the composition of calcium carbonate ($CaCO_3$) (Fig. 4*C*). In the utricle of *Slc26a4*^{loop} mutants, between one and several giant stones were found at all ages examined from P0 to 10 months old (Fig. 4, *D*, *G*, and *J*). These mineralized stones share similar morphological properties and the same composition of calcium carbonate ($CaCO_3$) (Fig. 4*F*). In the saccule, at P0, calcite minerals were also detected (Fig. 4*E*), but only in some of the cases. When a calcitic mineral was found, its size was smaller than that of utricular giant minerals. At the age of 7 months, *Slc26a4*$^{loop/loop}$ saccules contained an abnormal giant stone with a variety of morphological characteristics. SEM images showed that parts of this stone resemble the morphology of weddellite, calcium oxalate dihydrate (Fig. 4*H*, *inset*). By FTIR spectroscopy analysis, the calcite peak at 713 cm^{-1} is broadened relative to the same peak in wild type or in P0-P10 *Slc26a4*^{loop} mutants. This broadening reflects disorder in the calcite lattice (32); thus, at this stage, saccule *loop* minerals are mainly composed of highly disordered calcite (Fig. 4*I*). At the age of 10 months, the highly disordered calcite no longer appears and instead, a different type of giant stone with a symmetrical envelope shape, typical of weddellite crystals, is observed (Fig. 4*K*). FTIR confirmed that this mineral is composed of calcium oxalate dihydrate ($CaC_2O_4 \cdot 2H_2O$) in a form of weddellite (Fig. 4*L*). Micro-Raman spectroscopy ap-

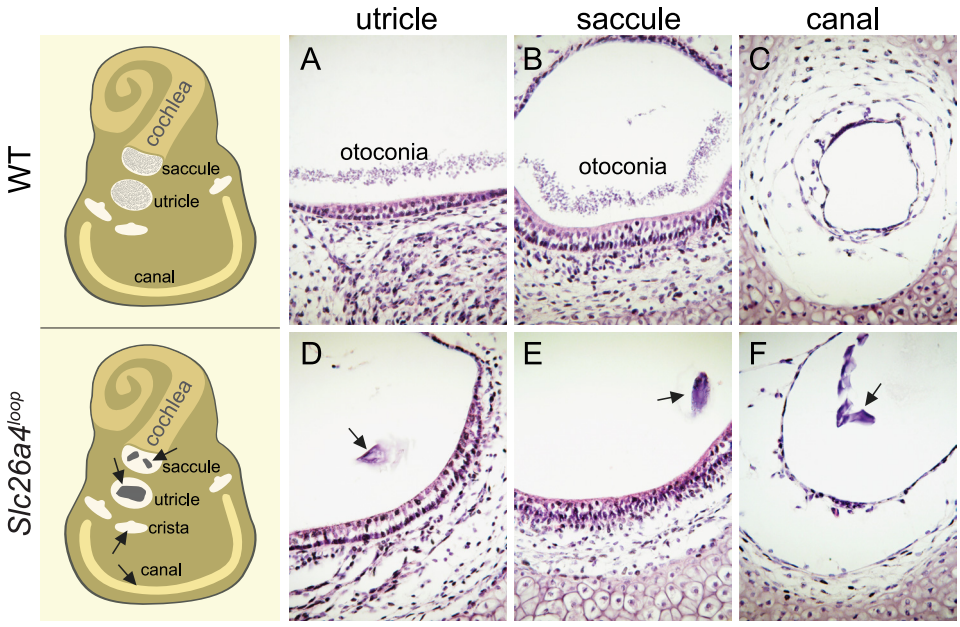

FIGURE 7. **Giant minerals are dislocated in *Slc26a4*$^{loop/loop}$ vestibular system.** A schematic representation of the inner ear (*left panels*) illustrates the possible positions of the ectopic mineralized bodies as found in a group of *Slc26a4*^{loop} mutant mice. *A–F*, histological paraffin sections from the vestibular system of P0 mice stained with hematoxylin and eosin. *A* and *B*, in wild-type mice, otoconia are restricted to the utricle and saccule, seen as a dense layer of tiny particles over the sensory epithelium. *C*, other endolymphatic compartments lack any otoconia, as demonstrated with a representative image of a semicircular canal. *D* and *E*, in *Slc26a4*^{loop} mutant mice, a giant mineral resides on top of the gravity receptors, utricle, and saccule. *F*, a frequent dislocation of the giant mineralized bodies to the semicircular canals and their cristae is observed. *Scale bars* equal 75 μm in *panels A–F*. $n = 4$.

plied to individually extracted minerals also confirmed these results (supplemental Fig. S3).

Ultrastructural Morphology of the Core and Surface of Slc26a4$^{loop/loop}$ *Mineralized Bodies*—Analysis of bisected calcitic mineralized bodies of the utricle revealed a smooth facet of the interior part, suggesting that the giant mineral develops from a single nucleation core rather than multiple otoconia assembly and joining (Fig. 5, *A* and *B*). Mineral properties are known to be affected by different environmental changes including physiological environment, temperature, and pH. Furthermore, kinetics of mineral dissolution is dependent on pH levels, which affects its surface hardness and microstructure (33). Thus, using SEM imaging, we analyzed the ultrastructural morphology of the mineralized surface of the giant stones isolated from the saccule of *Slc26a4*$^{loop/loop}$ at different ages (Fig. 5, *C--E*). At P0, the calcitic mineralized bodies showed a clean and smooth surface (Fig. 5*C*). However, at 7 months, the highly disordered calcite revealed a surface that is pitted and fissured (Fig. 5*D*). At 10 months, the calcium oxalate minerals had a smooth and planar surface (Fig. 5*E*).

Conglomerate of Otoconin-90 Assembles the Core Structure of the Giant Calcite Stones—Oc90 begins to be expressed 2 days prior to otoconia nucleation in the mouse, around E12.5, and has a critical role as the major core protein in otoconia development (9). To gain insight into the aberrant mineralization process observed in *Slc26a4*^{loop} mice, the Oc90 expression pattern in the mutant giant calcite minerals after otoconia maturation was analyzed. At P15, Oc90 is no longer expressed by the cells surrounding the macula. These cells extensively secrete this protein into the endolymph during early otoconia development (9). Later, the expression of Oc90 is trapped inside the wild-type otoconia, highlighting each otoconium boundary (Fig. 6*A*). The gap between the otoconia layer and the hair cell level (nuclei) in wild-type mice represents the gelatinous matrix (otoconial membrane) that supports the otoconia load (Fig. 6*A*). In *Slc26a4*$^{loop/loop}$ mice, Oc90 is expressed inside the giant mineral, seen as conglomerates, whereas the expression intensity is different along the body of the mineral (Fig. 6*B*). Moreover, the gap between the hair cells and the mineral no longer exists, and the giant stone lies directly on the sensory epithelium (Fig. 6*B*). Western blot analysis of the mineral fraction shows a dramatic increase in the levels of Oc90 in the giant calcitic minerals (Fig. 6*C*). To evaluate the integrity of the otoconial membrane, otogelin expression as a representative member of the gelatinous matrix proteins was examined. In wild-type mice, otogelin is expressed along the supporting cells within the sensory epithelium and in the otoconial membrane that carries the load of the otoconia (Fig. 6*D*). In *Slc26a4*$^{loop/loop}$ mice, otogelin expression appears to be normal in the supporting cells, but the otoconial membrane is severed and disorganized. Portions of the otoconia membrane are frequently detached from the maculae and displaced inside the gravity receptors (Fig. 6*E*, *arrow*).

Ectopic Distribution of Giant Minerals in Slc26a4$^{loop/loop}$ *Vestibular System*—In wild-type mice, otoconia scattered above the sensory epithelium of the saccule and the utricle (Fig. 7, *A* and *B*) are secured by a filamentous matrix (34) that prevents its dislocation. Hence, under normal conditions, otoconia are absent in other endolymphatic spaces (Fig. 7*C*). In *Slc26a4*^{loop} mutant mice, abnormal giant minerals are no longer restricted to their native position and are often observed in ectopic regions including the semicircular canals and their cristae (Fig. 7, *D–F*).

DISCUSSION

The small size of normal otoconia, together with their distribution pattern over the saccule and utricle, is crucial for generating an optimal mass over each individual hair cell, which is essential for their stimulation. Thus, the formation of giant minerals in *Slc26a4*$^{loop/loop}$ mutants leads to a differential mass over the sensory cells. Although some hair cells lack any otoconia load, other hair cells are overloaded with giant stones. Hence, both populations of hair cells are missing their native stimulation source and cannot serve their vital role in vestibular function and perception. Furthermore, the giant minerals in *Slc26a4*^{loop} mice are no longer restricted to the saccule or utri-

cle, as compared with normal otoconia. Ectopic giant stones were found in other components of the vestibular system such as the semicircular canals and their cristae. The variability of the defective vestibular behavior in *Slc26a4*^{loop} mutant mice, ranging from very mild to severe, can be partially explained by the variable position of dislocated mineralized bodies. It would be interesting to test this hypothesis and learn about possible correlations between the position of the stone and a specific vestibular defect. Displacement of otoconia in humans is associated with BPPV and leads to severe dizziness, imbalance, and nausea (35). The severe vertigo episodes are usually of a short duration and elicited by the position of the patient. A common way to treat BPPV is by maneuvering the free floating otoconia outside the semicircular canal and crista, providing the patient with relief (36–38). Hence, *Slc26a4*^{loop} mice can be tested as a platform for validating pioneering therapeutic approaches with respect to vestibular dysfunction as a result of otoconia dislocation.

Otoconia formation depends on organic and inorganic components that are secreted into an extracellular fluid and assembled to create a myriad of otoconia. The orchestrated expression of the genes involved in otoconia formation, together with the spatial and temporal abundance of the chemical elements, is crucial for proper otoconia assembly. Hence, depletion of components from the organic and inorganic parts of this equation can lead to otoconia defects. For example, deletion of the PMCA2 Ca^{2+} channel, a key player in establishing endolymph calcium homeostasis, results in a lack of otoconia formation (39). Alternatively, deletion of otoconin-90, the mammalian otoconial matrix protein, leads to formation of giant calcite minerals that lack the major organic fraction of otoconia (9, 40).

Pendrin is known to be expressed in the transitional cell layer surrounding the sensory epithelium of the saccule and utricle (41). Pendrin is a member in the SLC family of transporters and transports several different ions, including Cl^-, I^-, HCO_3^-, and formate (42–44). In the inner ear, pH measurements of the endolymph within the utricle of *Pds*$^{-/-}$ mice show acidification of the fluid (45, 46). Following these studies, pendrin was proposed to function as a Cl^-/HCO_3^- transporter in the inner ear that actively secretes

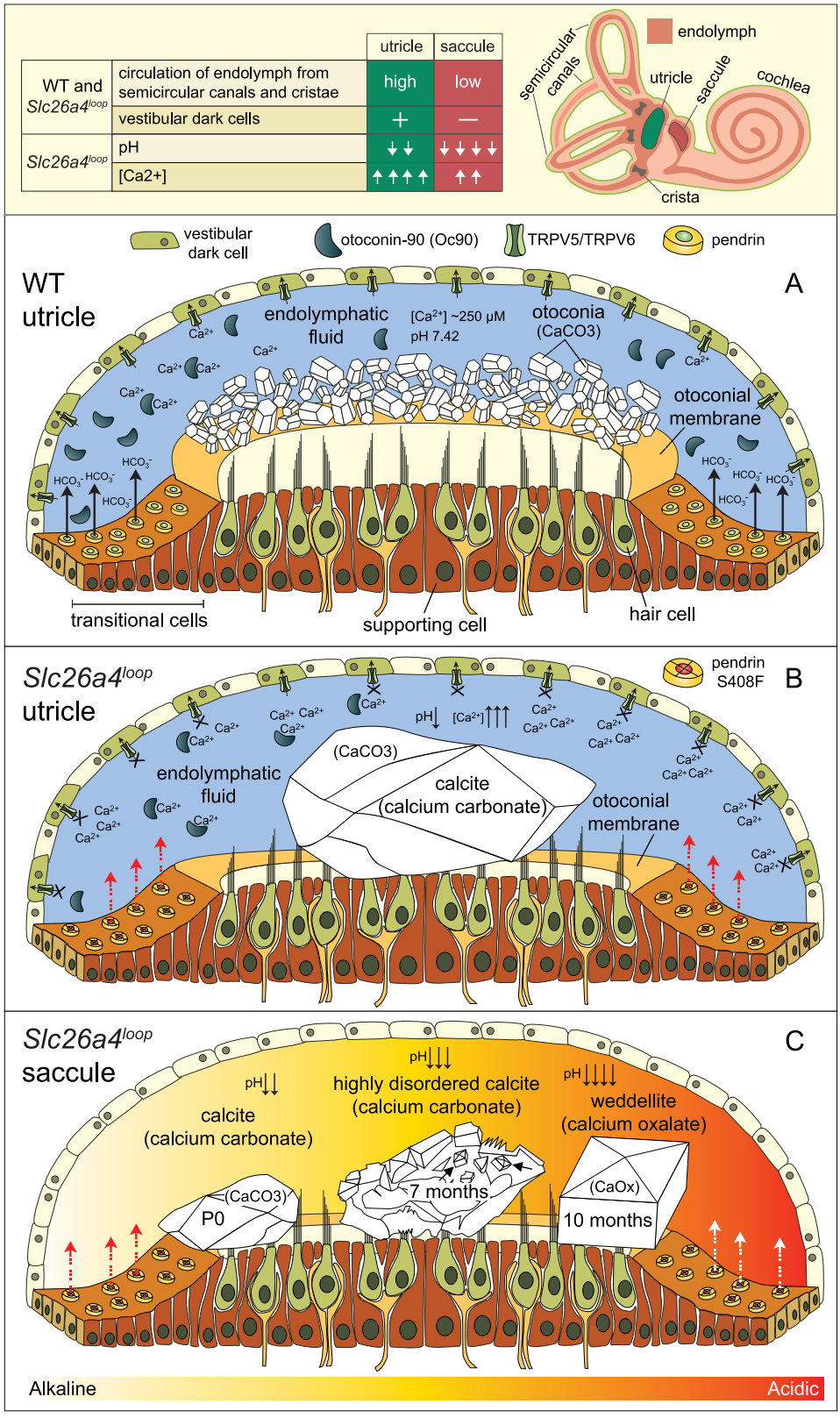

bicarbonate into the endolymph, which neutralizes H^+ and participates in buffering the normal physiological pH. Hence, control of appropriate pH levels is crucial for mineral assembly and stabilization. Pendrin may also be involved in otoconia formation by supplying HCO_3^- that is essential to form the calcite ($CaCO_3$) crystals of otoconia. However, the extensive mineral growths observed in the utricle of *Slc26a4*^{loop} mutants early in development suggests that the reservoir of bicarbonate for otoconia assembly was not reduced drastically. A putative compensation for loss of bicarbonate is achieved by the activity of carbonic anhydrase due to its production of HCO_3^- and H^+ from CO_2 and H_2O. This enzyme is known to be widely expressed in sensory and non-sensory epithelia of the utricle and saccule (47, 48).

This work has demonstrated how a missense mutation (S408F) within a highly conserved region of the pendrin protein leads to impaired transport activity. We also report that this defective mutation leads to differential defects in otoconia formation between the utricle and saccule of *Slc26a4*^{loop} mutants. Although abnormal giant calcite minerals always reside in *Slc26a4*$^{loop/loop}$ utricles, a gradual change in mineral composition is observed in the saccule, with formation of calcium oxalate stones in adult mice. These giant minerals, irrespective of shape and composition, can no longer serve their vital and elementary role in proper hair cell stimulation and vestibular function. Interestingly, these differential mineralization defects occur despite the similar pattern of pendrin expression in the saccule and utricle. Our findings also suggest that the minerals in the utricle and saccule are exposed to different endolymphatic environments. We predict that abolished activity of pendrin in *Slc26a4*^{loop} mutants leads to different levels of acidification in each of the these two compartments. Hence, anatomical and histological differences between utricle and saccule, together with pH-sensitive proteins that are differentially expressed in these maculae, may be the key for understanding the mechanism underlying this complex pathology.

Initial Formation of Giant Calcium Carbonate Stones in Slc26a4$^{loop/loop}$ *Vestibule*—The similarity between the utricle and saccule is striking. Both are sensitive for linear acceleration, have otoconia as an inertial mass for stimulation initiation, and contain the same type of sensory hair cells. However, several distinct anatomical and histological characteristics are unique to each of these maculae. The differences between utricle and saccule are illustrated (Fig. 8, *top panel*) and include two main aspects pertaining to the current discussion. First, the endolymph of the utricle is connected to the semicircular canals and the crista ampullaris and share fluid circulation with these vestibular components, as opposed to the saccule, which lacks this direct connection. Second, a pronounced difference is the large abundance of the pigmented vestibular dark cells in the utricle but absent in the saccule.

Previous studies on the *Pds*$^{-/-}$ mice show that the acidification of the vestibular endolymph inhibits the pH-sensitive calcium channels, TRPV5 and TRPV6 (46, 49). Both TRPV5 and TRPV6 were shown to be expressed in the vestibular dark cells and in the epithelial cells of the semicircular canal duct epithelium (50, 51). The abolished calcium reabsorbance of these channels leads to elevation in calcium levels in the endolymph to which the utricle is exposed. Under normal conditions, the calcium concentration in the endolymph is very low as compared with other physiological fluids. The low calcium level is essential for the mechanotransduction machinery of the sensory hair cells (52). One way to maintain this environment is achieved by calcium absorbance of the surrounding epithelial cells. Another way to control calcium levels is by recruiting calcium for otoconia formation, which was proposed to be a method for providing a calcium reservoir (53). A key player in this respect is Oc90, which sequesters calcium ions. In wild-type mice, Oc90 is secreted into the endolymph prior to otoconia nucleation and participates in the growth of these tiny minerals (1, 9). Under normal conditions, the secreted amount of Oc90 competes with a normally low level of calcium ions and is thus essential for the initial nucleation of otoconia. The level of Oc90 expression and secretion into the endolymph of *Slc26a4*^{loop} mutants is most likely not affected by the pendrin S408F mutation. However, there is a dramatic increase in the amount of Oc90 that is observed in the giant mineral of *Slc26a4*$^{loop/loop}$ mice as compared with the wild-type otoconia. This discrepancy can be explained by the presumed higher calcium levels in the endolymph of *Slc26a4*^{loop} mutants, which leads to rapid trapping of any residual Oc90 into a giant crystal.

Taken together, elevation of calcium levels in the endolymph fluid, within the common compartment of the utricle, cristae, and semicircular canals, leads to a differential calcium concentration between utricle and saccule, with higher calcium levels in the utricle. The formation of giant calcitic stones in the utricle and significantly smaller stones in the saccule can be attributed to differences in calcium concentration. Furthermore, this

FIGURE 8. **Proposed working model for calcium oxalate stone formation in the inner ear.** The anatomical differences (*top panels*) between the utricle (*green*) and saccule (*red*) are illustrated and summarized in a table. *A*, under normal conditions, otoconia nucleation begins around E16.5 and reaches its maturation at P7. To support the biomineralization events, otoconia proteins such as Oc90 are secreted to the endolymph prior to and during otoconia nucleation and maturation. *B*, in *Slc26a4*^{loop} mice, the organic fraction of otoconia, including Oc90, is secreted normally to the extracellular space, but the homeostasis of the endolymph is impaired. Pendrin activity is depleted due to the S408F mutation, and the lack of HCO_3^- supply leads to acidification of the endolymphatic fluids. This acidification abolishes the reabsorption of calcium by the pH-sensitive calcium channels, TRPV5 and TRPV6 (46). The localization of TRPV5 and TRPV6 in the semicircular canal duct epithelium and in the vestibular dark cells, which share fluid circulation with the utricle, leads to a higher calcium concentration in the utricle as compared with the saccule. The excess calcium ions in the endolymph of the utricle are sequestered by large amounts of Oc90 and deposited into oversized calcite minerals, whereas in the saccule, significantly smaller minerals are formed. *C*, at progressive ages, wild-type otoconia are maintained with low calcium turnover, whereas in *Slc26a4*^{loop} mice, a differential process between saccule and utricle occurs. In the utricle, giant calcitic minerals reside all along the lifespan of the mouse. In the saccule, a gradual change in mineral morphology and composition from calcite into highly disordered calcite at the age of 7 months is observed. The ultrastructural morphology of the highly disordered mineral, a pitted and fissured surface, resembles the morphology of calcite mineral after treatment with an acidic solution. Moreover, this stone contained domains that resembled the morphology of calcium oxalate in the form of weddellite. Between the age of 7 and 10 months, the highly disordered calcite dissolved, and giant calcium oxalate minerals in the form of weddellite were generated. The symmetrical morphology of the weddellite resembles the classical calcium oxalate geological mineral, which is more stable at lower pH as compared with the calcium carbonate. In summary, constant acidification of the saccule leads to dissolution of the calcite mineral that is tied with favorable conditions for calcium oxalate stone formation in the inner ear.

postulated difference in the level of calcium may be connected to the observation that one giant mineralized body forms in the mutants, instead of many small uniformly sized and shaped otoconia in the wild-type mice. It is conceivable that because of the high calcium concentrations in the *Slc26a4*$^{loop/loop}$ endolymph, the first nucleated otoconia continues to grow rapidly and sequesters most of the calcium. Any other small crystals that may subsequently form would redissolve because of the lack of calcium in their microenvironment.

The data presented in this study are confined to postnatal stages. Several models have been proposed in the literature for early otoconia seeding and maturation (5, 54). Although one model suggests secretion of vesicles with otoconia substances as a seeding platform (55, 56), a second model excludes involvement of vesicles as otoconia precursors and proposes that perimacular seeding occurs following temporal and spatial secretion of individual otoconia components (54). The core structure of the giant calcitic mineralized bodies in *Slc26a4*^{loop} mutants suggests that these giant stones are developing from a single nucleation core with continued growth rather than multiple assembly of thousands of mature otoconia particles. Observation of E15.5 utricles reveals that the aberrant giant mineral already exists at this stage (data not shown) and supports our assumption. Further characterization of the early developmental steps that initiate the growth of these giant minerals can provide important clues with respect to the proposed models of otoconia development.

Drastic Changes in Mineral Morphology and Composition in Slc26a4$^{loop/loop}$ *Saccule*—Mineral properties are affected by different environmental changes, including temperature and pH. Kinetics of mineral dissolution is dependent on pH levels, which affects its surface hardness and microstructure (33). As a consequence of endolymph circulation in the utricle, the volume of endolymph to which the utricle is exposed to is larger than that of the saccule. Therefore, the reduction in endolymphatic pH, following abnormal activity of pendrin, is presumed to be mild in the utricle where the endolymph is circulated frequently. However, in the saccule of *Slc26a4*^{loop} mutants, which lacks this pronounced circulation, a lower pH level is expected to develop. We revealed a progressive gradual change in mineral morphology and composition in the saccule of *Slc26a4*^{loop} mutants. Furthermore, the structure of these minerals suggests that a gradual reduction in pH of the saccule endolymph develops with age. In newborns, small calcium carbonate minerals in the form of calcite rarely developed. However, at the age of 7 months, a giant, highly disordered calcium carbonate mineral in the form of calcite was apparent. An ultrastructural analysis of this mineral revealed a pitted and fissured surface, resembling the pattern of calcite mineral after exposure to an acidic solution. Significantly, this stone contained weddellite. At the age of 10 months, the highly disordered calcite was no longer found, and instead, giant calcium oxalate stones in the form of weddellite were detected. Biosynthesis of oxalate from carbonate is not known *in vitro*. Hence, we suggest that the highly disordered calcite is unstable due to the constant acidification of the environment, and this results in mineral dissolution. Consequently, the endolymphatic environment is enriched with calcium ions, which now bind to oxalate ions and subsequently precipitate as calcium oxalate crystals in the form of weddellite. The symmetrical morphology of the weddellite resembles the classical calcium oxalate geological mineral, which is more stable at lower pH as compared with the calcium carbonate. Thus, acidification of the saccule fluids is in favor of calcium oxalate mineral formation (summarized in Fig. 8). Pendrin is capable of transporting formate but not oxalate (42). We hypothesize that the S408F mutation might alter the affinity of pendrin transport to oxalate, which is chemically closely related to formate. Additional experiments we performed with the fast fluorometric approach to test this hypothesis suggest that the S408F mutation does not impose a new function of oxalate transport by the pendrin protein *in vitro* (data not shown). Formation of calcium oxalate minerals is also known in kidney pathology and accounts for more than 80% of kidney stones (57). Thus, because pendrin is widely expressed in the cortical collecting duct of the kidney (58), we investigated the possibility of kidney stone formation using Pizzolato's staining for oxalate deposits (59). Histological analysis of *Slc26a4*$^{loop/loop}$ kidney up to the age of 10 months did not reveal oxalate stone accumulation (data not shown). In healthy individuals, most of the crystals that are formed in the renal tubules are discharged in the urine. However, the inner ear is a closed fluid-filled compartment that lacks fluid circulation with other systems in the body. Thus, when oxalate crystals are precipitated in the inner ear, they are trapped within the endolymph, and their accumulation and aggregation are inevitable. This aberrant genetic-dependent mineralization process that leads to calcium oxalate stones formation is described in the mammalian ear for the first time.

Acknowledgments—We thank Jørgen Frøkiær and Christine Petit for antibodies and Leonid Mittelman for training in confocal microscopy.

REFERENCES

1. Thalmann, R., Ignatova, E., Kachar, B., Ornitz, D. M., and Thalmann, I. (2001) *Ann. N.Y. Acad. Sci.* **942,** 162–178
2. Carlström, D. (1963) *Biol. Bull.* **125,** 441–463
3. Berman, A., Addadi, L., and Weiner, S. (1988) *Nature* **331,** 546–548
4. Lowenstam, H., and Weiner, S. (1989) *On Biomineralization*, Oxford University Press, New York, NY
5. Hughes, I., Thalmann, I., Thalmann, R., and Ornitz, D. M. (2006) *Brain Res.* **1091,** 58–74
6. Anniko, M. (1980) *Am. J. Otolaryngol.* **1,** 400–410
7. Erway, L. C., Purichia, N. A., Netzler, E. R., D'Amore, M. A., Esses, D., and Levine, M. (1986) *Scan. Electron. Microsc.* **4,** 1681–1694
8. Ross, M. D., and Peacor, D. R. (1975) *Ann. Otol. Rhinol. Laryngol.* **84,** 22–36
9. Verpy, E., Leibovici, M., and Petit, C. (1999) *Proc. Natl. Acad. Sci. U.S.A.* **96,** 529–534
10. Wang, Y., Kowalski, P. E., Thalmann, I., Ornitz, D. M., Mager, D. L., and Thalmann, R. (1998) *Proc. Natl. Acad. Sci. U.S.A.* **95,** 15345–15350
11. Pote, K. G., Hauer, C. R., 3rd, Michel, H., Shabanowitz, J., Hunt, D. F., and Kretsinger, R. H. (1993) *Biochemistry* **32,** 5017–5024
12. Pote, K. G., and Ross, M. D. (1991) *Comp. Biochem. Physiol. B* **98,** 287–295
13. Takumida, M., Zhang, D. M., Yajin, K., and Harada, Y. (1997) *Acta Otolaryngol.* **117,** 538–544
14. Harada, Y., and Sugimoto, Y. (1977) *Acta Otolaryngol.* **84,** 65–71
15. Ross, M. D., Peacor, D., Johnsson, L. G., and Allard, L. F. (1976) *Ann. Otol. Rhinol. Laryngol.* **85,** 310–326
16. Oghalai, J. S., Manolidis, S., Barth, J. L., Stewart, M. G., and Jenkins, H. A. (2000) *Otolaryngol. Head Neck Surg.* **122,** 630–634

17. House, M. G., and Honrubia, V. (2003) *Audiol. Neurootol.* **8,** 91–99
18. Coyle, B., Coffey, R., Armour, J. A., Gausden, E., Hochberg, Z., Grossman, A., Britton, K., Pembrey, M., Reardon, W., and Trembath, R. (1996) *Nat. Genet.* **12,** 421–423
19. Sheffield, V. C., Kraiem, Z., Beck, J. C., Nishimura, D., Stone, E. M., Salameh, M., Sadeh, O., and Glaser, B. (1996) *Nat. Genet.* **12,** 424–426
20. Hertzano, R., Shalit, E., Rzadzinska, A. K., Dror, A. A., Song, L., Ron, U., Tan, J. T., Shitrit, A. S., Fuchs, H., Hasson, T., Ben-Tal, N., Sweeney, H. L., de Angelis, M. H., Steel, K. P., and Avraham, K. B. (2008) *PLoS Genet.* **4,** e1000207
21. Simmler, M. C., Cohen-Salmon, M., El-Amraoui, A., Guillaud, L., Benichou, J. C., Petit, C., and Panthier, J. J. (2000) *Nat. Genet.* **24,** 139–143
22. Frische, S., Kwon, T. H., Frøkiaer, J., Madsen, K. M., and Nielsen, S. (2003) *Am. J. Physiol. Renal Physiol.* **284,** F584–F593
23. Cohen-Salmon, M., El-Amraoui, A., Leibovici, M., and Petit, C. (1997) *Proc. Natl. Acad. Sci. U.S.A.* **94,** 14450–14455
24. Hunter-Duvar, I. M. (1978) *Acta Otolaryngol. Suppl.* **351,** 3–23
25. Fugazzola, L., Cirello, V., Dossena, S., Rodighiero, S., Muzza, M., Castorina, P., Lalatta, F., Ambrosetti, U., Beck-Peccoz, P., Bottà, G., and Paulmichl, M. (2007) *Eur. J. Endocrinol.* **157,** 331–338
26. DiCiommo, D. P., Duckett, A., Burcescu, I., Bremner, R., and Gallie, B. L. (2004) *Invest Ophthalmol. Vis. Sci.* **45,** 3320–3329
27. Dossena, S., Rodighiero, S., Vezzoli, V., Bazzini, C., Sironi, C., Meyer, G., Fürst, J., Ritter, M., Garavaglia, M. L., Fugazzola, L., Persani, L., Zorowka, P., Storelli, C., Beck-Peccoz, P., Bottá, G., and Paulmichl, M. (2006) *Cell Physiol. Biochem.* **18,** 67–74
28. Dossena, S., Rodighiero, S., Vezzoli, V., Nofziger, C., Salvioni, E., Boccazzi, M., Grabmayer, E., Bottà, G., Meyer, G., Fugazzola, L., Beck-Peccoz, P., and Paulmichl, M. (2009) *J. Mol. Endocrinol.* **43,** 93–103
29. Pera, A., Dossena, S., Rodighiero, S., Gandía, M., Bottà, G., Meyer, G., Moreno, F., Nofziger, C., Hernández-Chico, C., and Paulmichl, M. (2008) *Proc. Natl. Acad. Sci. U.S.A.* **105,** 18608–18613
30. Jayaraman, S., Haggie, P., Wachter, R. M., Remington, S. J., and Verkman, A. S. (2000) *J. Biol. Chem.* **275,** 6047–6050
31. Everett, L. A., Belyantseva, I. A., Noben-Trauth, K., Cantos, R., Chen, A., Thakkar, S. I., Hoogstraten-Miller, S. L., Kachar, B., Wu, D. K., and Green, E. D. (2001) *Hum. Mol. Genet.* **10,** 153–161
32. Beniash, E., Aizenberg, J., Addadi, L., and Weiner, S. (1997) *Proc. Biol. Sci.* **264,** 461–465
33. Sjöberg, E. L., and Rickard, D. T. (1984) *Geochim. Cosmochim. Acta* **48,** 485–493
34. Lins, U., Farina, M., Kurc, M., Riordan, G., Thalmann, R., Thalmann, I., and Kachar, B. (2000) *J. Struct. Biol.* **131,** 67–78
35. Epley, J. M. (1995) *Otolaryngol. Head Neck Surg.* **112,** 154–161
36. Beynon, G. J. (1997) *Br. J. Audiol.* **31,** 11–26
37. Epley, J. M. (1992) *Otolaryngol. Head Neck Surg.* **107,** 399–404
38. Parnes, L. S., Agrawal, S. K., and Atlas, J. (2003) *CMAJ* **169,** 681–693
39. Kozel, P. J., Friedman, R. A., Erway, L. C., Yamoah, E. N., Liu, L. H., Riddle, T., Duffy, J. J., Doetschman, T., Miller, M. L., Cardell, E. L., and Shull, G. E. (1998) *J. Biol. Chem.* **273,** 18693–18696
40. Zhao, X., Yang, H., Yamoah, E. N., and Lundberg, Y. W. (2007) *Dev. Biol.* **304,** 508–524
41. Royaux, I. E., Belyantseva, I. A., Wu, T., Kachar, B., Everett, L. A., Marcus, D. C., and Green, E. D. (2003) *J. Assoc. Res. Otolaryngol.* **4,** 394–404
42. Scott, D. A., and Karniski, L. P. (2000) *Am. J. Physiol. Cell Physiol.* **278,** C207–C211
43. Scott, D. A., Wang, R., Kreman, T. M., Sheffield, V. C., and Karniski, L. P. (1999) *Nat. Genet.* **21,** 440–443
44. Soleimani, M., Greeley, T., Petrovic, S., Wang, Z., Amlal, H., Kopp, P., and Burnham, C. E. (2001) *Am. J. Physiol. Renal Physiol.* **280,** F356–F364
45. Wangemann, P., Nakaya, K., Wu, T., Maganti, R. J., Itza, E. M., Sanneman, J. D., Harbidge, D. G., Billings, S., and Marcus, D. C. (2007) *Am. J. Physiol. Renal Physiol.* **292,** F1345–1353
46. Nakaya, K., Harbidge, D. G., Wangemann, P., Schultz, B. D., Green, E. D., Wall, S. M., and Marcus, D. C. (2007) *Am. J. Physiol. Renal Physiol.* **292,** F1314–F1321
47. Shiao, J. C., Lin, L. Y., Horng, J. L., Hwang, P. P., and Kaneko, T. (2005) *J. Comp. Neurol.* **488,** 331–341
48. Lim, D. J., Karabinas, C., and Trune, D. R. (1983) *Am. J. Otolaryngol.* **4,** 33–342
49. Yeh, B. I., Sun, T. J., Lee, J. Z., Chen, H. H., and Huang, C. L. (2003) *J. Biol. Chem.* **278,** 51044–51052
50. Takumida, M., Ishibashi, T., Hamamoto, T., Hirakawa, K., and Anniko, M. (2009) *Acta Otolaryngol.* **129,** 1340–1350
51. Yamauchi, D., Raveendran, N. N., Pondugula, S. R., Kampalli, S. B., Sanneman, J. D., Harbidge, D. G., and Marcus, D. C. (2005) *Biochem. Biophys. Res. Commun.* **331,** 1353–1357
52. Marquis, R. E., and Hudspeth, A. J. (1997) *Proc. Natl. Acad. Sci. U.S.A.* **94,** 11923–11928
53. Ross, M. D. (1979) *Adv. Otorhinolaryngol.* **25,** 26–33
54. Lundberg, Y. W., Zhao, X., and Yamoah, E. N. (2006) *Brain Res.* **1091,** 47–57
55. Suzuki, H., Ikeda, K., and Takasaka, T. (1995) *Hear Res.* **90,** 212–218
56. Suzuki, H., Ikeda, K., Furukawa, M., and Takasaka, T. (1997) *Am. J. Physiol.* **273,** C1533–C1540
57. Moe, O. W. (2006) *Lancet* **367,** 333–344
58. Royaux, I. E., Wall, S. M., Karniski, L. P., Everett, L. A., Suzuki, K., Knepper, M. A., and Green, E. D. (2001) *Proc. Natl. Acad. Sci. U.S.A.* **98,** 4221–4226
59. Pizzolato, P. (1964) *J. Histochem. Cytochem.* **12,** 333–336
60. Krogh, A., Larsson, B., von Heijne, G., and Sonnhammer, E. L. (2001) *J. Mol. Biol.* **305,** 567–580
61. Juretić, D., Zoranić, L., and Zucić, D. (2002) *J. Chem. Inf. Comput. Sci.* **42,** 620–632
62. Berezin, C., Glaser, F., Rosenberg, J., Paz, I., Pupko, T., Fariselli, P., Casadio, R., and Ben-Tal, N. (2004) *Bioinformatics* **20,** 1322–1324
63. Hrabé de Angelis, M. H., Flaswinkel, H., Fuchs, H., Rathkolb, B., Soewarto, D., Marschall, S., Heffner, S., Pargent, W., Wuensch, K., Jung, M., Reis, A., Richter, T., Alessandrini, F., Jakob, T., Fuchs, E., Kolb, H., Kremmer, E., Schaeble, K., Rollinski, B., Roscher, A., Peters, C., Meitinger, T., Strom, T., Steckler, T., Holsboer, F., Klopstock, T., Gekeler, F., Schindewolf, C., Jung, T., Avraham, K., Behrendt, H., Ring, J., Zimmer, A., Schughart, K., Pfeffer, K., Wolf, E., and Balling, R. (2000) *Nat. Genet.* **25,** 444–447